

# Multicellular Tumor Spheroid in an off-lattice Voronoi/Delaunay cell model

Gernot Schaller

*Institut für Theoretische Physik, Technische  
Universität Dresden, D-01062 Dresden, Germany\**

Michael Meyer-Hermann

*Centre for Mathematical Biology, Mathematical Institute,  
24-29 St. Giles', Oxford University,  
Oxford OX1 3LB, United Kingdom*

(Dated: December 2, 2024)

## Abstract

We study multicellular tumor spheroids by introducing a new three-dimensional agent-based Voronoi/Delaunay hybrid model. In this model, the cell shape varies from spherical in thin solution to convex polyhedral in dense tissues. The next neighbors of the cells are provided by a weighted Delaunay triangulation with in average linear computational complexity. The cellular interactions include direct elastic forces and cell-cell as well as cell-matrix adhesion. The spatiotemporal distribution of two nutrients – oxygen and glucose – is described by reaction-diffusion equations. Viable cells consume the nutrients, which are converted into biomass by increasing the cell size during  $G_1$ -phase.

We test hypotheses of the functional dependence of the uptake rates and use the computer simulation to find suitable mechanisms for induction of necrosis. This is done by comparing the outcome with experimental growth curves, where the best fit leads to an unexpected ratio of oxygen and glucose uptake rates. The model relies on physical quantities and can easily be generalized towards tissues involving different cell types. In addition, it provides many features that can be directly compared with the experiment.

PACS numbers: 45.05.+x, 82.30.-b, 87.\*, 02.70.-c

---

\*Electronic address: schaller@theory.phy.tu-dresden.de

## I. INTRODUCTION

The spatiotemporal dynamics of individual cells often leads to the emergence of fascinating complex patterns in cellular tissues. For example, during embryogenesis it is hypothesized that these complex patterns develop with the aid of mechanisms such as diffusing messengers and cell-cell contact. Sometimes these patterns can be described very well with a simple model. Such mathematical models can help to test hypotheses in in-silico experiments thereby circumventing real experiments which are very often expensive and time-consuming. However, since the local nature of cell-cell interactions is not precisely known one is often restricted to compare the global outcome following from different hypotheses with experimental data. Unfortunately, there are – unlike in theoretical physics – no established first principle theories in cell tissue modeling which explains that there is a variety of models on the market, which can be classified as follows:

Firstly, there is a class of models where one derives continuum equations for the cell populations. In analogy to many-particle physics one replaces the actual information on every cell by a cellular density. Consequently, the equations of motion can be simplified considerably to a differential equation describing the spatiotemporal dynamics of a cell type. In practice these equations do very often have the type of reaction-diffusion equations [1]. The volume-integral of such equations results in the global dynamics of a whole population (e.g. predator-prey-models), where only the temporal development of the total population is monitored. Note however, that cellular interactions can only be modeled effectively with these approaches. Also, the discrete and individual nature of cells is completely neglected.

The discrete nature can be taken into account by deriving master equations for the population number on every volume element [2]. By mapping these master equations to a Schrödinger equation one is able to identify an Hamilton operator that allows a physicist to apply the mathematical framework of quantum field theory to systems such as cell tissues. For example, in the simple case of Lotka-Volterra equations [1] this method leads to mean-field equations that resemble the Lotka-Volterra equations. The renormalized numerical results [3] however disagree with the mean-field approximations. Consequently, the discrete nature of cells may not always be neglected. Still, the above quantization assumes all agents to be identical and indistinguishable and inevitably neglects the individuality of cells. Therefore, features such as cell shape and differences in cell size or internal properties

are not considered in this class of models.

This is different in the third class of agent-based models, where cells are represented by individually interacting objects. Since now every single cell must be included in the computer simulations the computational intensity increases considerably. This however opens often the possibility to choose the interaction rules intuitively from existing observations. These models are usually restricted to a certain cell shape, which enables one to sub-classify them further: In lattice-based models [4, 5] the cellular shape is usually already defined by the shape of the elementary cell of the lattice, such as e.g. cubic [6] or hexagonal [7, 8]. Off-lattice models usually restrict to one special cell form and consider slight perturbations (e.g. deformable spheres [9, 10] or deformable ellipsoids [11, 12, 13]). In other off-lattice models the geometrical Voronoi tessellation [14, 15] is used, which allows for more variations in cell shape and size. In addition, it comes very close to the polyhedral shape observed for some cell types [16]. An important advantage of off-lattice models is that perturbations from the inert cell shape can give rise to physically well-defined cellular interaction forces, whereas in lattice-based models one is usually forced to introduce effective interaction rules which makes it difficult to relate the model parameters to experimentally accessible quantities.

Since cell shape and function are usually closely connected (e. g. fibroblasts in the human skin do have a different shape than melanocytes or keratinocytes), there are some models that try to reproduce any possible cell shape. For example in the extended Potts model [17, 18, 19, 20] one has spins on several lattice nodes describing a single cell. The dynamics of these spins is calculated with a Hamiltonian approach. The parameters in this Hamilton operator however are often difficult to relate to physically measurable quantities. This problem is circumvented in force-based models. For example in [21] the relation of cell shape and cell motility has been investigated in a model that represents cells as a collection of cell fragments on a lattice. Other force-based models [22, 23] describe cell shape on a 2-dimensional hypersurface by a changing number of polygonal nodes, which is also computationally expensive. These models always need a large number of general coordinates to define the shape or status of a cell and are therefore restricted to a relatively small number of cells – even at present computational power.

Balancing these reasons in the context of the aimed description of in vitro tumor growth data we decided to use an off-lattice agent-based model, where one has the advantage of allowing continuous cell positions. Therefore the extent by which cellular interactions have

to be replaced by effective automaton rules is much smaller than in corresponding cellular automata [7]. In addition, the model parameters can be directly measured in independent experiments. The enormous computational intensity common to most existing off-lattice models is due to two effects: Firstly, some off-lattice models [5] use effective stochastic interaction rules, which require stochastic solution methods such as the Metropolis algorithm. The infinite number of possibilities in a continuous model however requires a large part of the phase space to be tested. Secondly, the determination of the neighborhood topology for local interactions requires sophisticated algorithms. Our model uses the weighted Delaunay triangulation which provides the correct neighborhood topology for a set of spheres with different radii with in average constant access. In addition, the model is dominantly deterministic which abolishes the necessity to test irrelevant parts of the phase space.

Unlike in two dimensions, where tumor cells in in-vitro setups will proliferate without limitation, there exist growth limitations on tumor cell populations forming solid spheroidal cell aggregates in three dimensions [24]. This limitation of growth is presumably due to both contact inhibition – which is also active in two dimensions [10] – and nutrient depletion in the interior of the spheroid. Initially, the cell number grows exponentially and enters a polynomial growth phase after some days in culture. Finally, a saturation of growth is observed for many spheroid systems [25]. The final stages of spheroid growth exhibit a typical pattern in the cross-sections: An internal necrotic core is surrounded by a layer of quiescent cells – which do not proliferate – and on the outside one has a layer of proliferating cells [26]. The final stage depends critically on the supply with nutrients such as oxygen and glucose. The model we have implemented enables us to model  $\mathcal{O}(10^5)$  cells which is in agreement with cell numbers observed in multicellular tumor spheroid systems [25]. We will demonstrate that the growth curves measured in [25] for different nutrient concentrations can be reproduced using a single parameter set and simple assumptions for cellular interactions.

## II. THE CELL MODEL

In our model we assume cells to be deformable spheres with dynamic radii, which is motivated by the experimental observation that cells in a solution tend to be spherical – presumably in order to minimize their surface energy. Consequently, we treat all deviations from this spherical form as perturbations from the inert cellular shape.

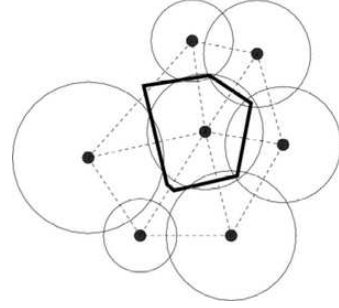
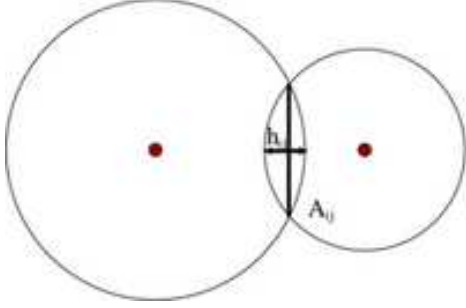


FIG. 1: Two-dimensional illustration of inter-  
penetrating spheres with maximum overlap  $h_{ij}$   
and sphere contact surface  $A_{ij}$ . In reality, the  
spheres will deform and generate a repulsive  
force.

FIG. 2: Within dense tissues, many-sphere-  
overlaps can occur. In this case, the weighted  
Voronoi tessellation (marked with a bold line)  
provides a more realistic estimate of the cellu-  
lar contact surfaces.

The model is agent-based (sometimes also called individual-based), i. e. every biological cell is represented by an individual object. These objects interact locally with their next neighbors (those that follow from the weighted Delaunay triangulation) and with a reaction-diffusion grid (for nutrients or growth signals). Each cell is characterized by several individual parameters such as position and a radius, the type corresponding to biological classifications, the status (position in the cell cycle), cellular tension, receptor and ligand concentrations on the cell membrane, an internal clock, and cell-type specific coupling constants for elastic and adhesive interactions. Since we assume the inert cell shape to be spherical, the power-weighted Delaunay triangulation [15] is a perfect tool to determine the neighborhood topology.

### A. Elastic and adhesive Cell-Cell interactions

Following a model of Hertz [27, 28] – which has already been used in the framework of cell tissues [10, 29] – the absolute value of the elastic force between two spheres with radii  $R_i$  and  $R_j$  can, for small deformations, be described as

$$F_{ij}^{\text{el}} = \frac{h_{ij}^{3/2}}{\frac{3}{4} \left( \frac{1-\nu_i^2}{E_i} + \frac{1-\nu_j^2}{E_j} \right) \sqrt{\frac{1}{R_i} + \frac{1}{R_j}}}, \quad (1)$$

where  $E_{i/j}$  and  $\nu_{i/j}$  represent the elasticities and Poisson ratios of the spheres, respectively. The quantity  $h_{ij} = \max\{0, R_i + R_j - |\mathbf{r}_i - \mathbf{r}_j|\}$  represents the maximum overlap the spheres

would have if they would not deform but interpenetrate each other, see figure 1.

In reality this model might not be adequate for cells: Firstly, the mechanics of the cytoskeleton is not well represented which might yield other than purely elastic responses (see e. g. [13, 30]). Secondly, equation (1) represents only a first order approximation which is valid for small virtual overlaps  $h_{ij} \ll \min\{R_i, R_j\}$  only. A more exact approach would be to follow [11, 12] by replacing cells by equivalent networks containing elastic and viscous elements. However, the parameters required for this model should either be measured for every cell type independently or they should be derived from a microscopic model of the cytoskeleton such as e.g. tensegrity structures [31, 32], which is beyond the scope of this article. We would like to restrict to the simple model (1), since it allows the independently measurable experimental quantities  $\nu_i$  and  $E_i$  to be directly included.

Intercellular adhesion in a tissue is mediated by receptor and ligand molecules that are distributed on the cell membranes. We neglect a possible dynamical clustering of adhesion molecules and assume them to be uniformly distributed. The resulting adhesive forces between two cells should then scale with their contact area  $A_{ij}$  (see also e. g. [11]) and can be estimated as

$$F_{ij}^{\text{ad}} = A_{ij} f^{\text{ad}} \frac{1}{2} \left( c_i^{\text{rec}} c_j^{\text{lig}} + c_i^{\text{lig}} c_j^{\text{rec}} \right), \quad (2)$$

where the receptor and ligand concentrations  $c_i^{\text{rec/lig}}$  are assumed to be normalized (i. e.  $0 \leq c_i^{\text{rec/lig}} \leq c_i^{\text{rec/lig:max}} \leq 1$ ) without loss of generality, since the – globally valid – coupling constant  $f^{\text{ad}}$  can always be rescaled. The contact surface area  $A_{ij}$  can be estimated using the contact surface of two overlapping spheres  $A_{ij}^{\text{sphere}}$  – see figure 1. In dense tissues however, this is not a valid description anymore, since the contact surfaces of many spheres might overlap as in figure 2 inferring double-counting of surfaces and thus overestimating of the total cell surface.

The weighted Voronoi tessellation [15, 33] of a set of spheres  $\{\mathbf{r}_i, R_i\}$

$$V_i = \{ \mathbf{x} \in \mathbb{R}^n : (\mathbf{x} - \mathbf{r}_i)^2 - R_i^2 \leq (\mathbf{x} - \mathbf{r}_j)^2 - R_j^2, \forall j \neq i \}, \quad (3)$$

divides space into Voronoi regions – convex polyhedra that may in some sense be associated with the space occupied by cell  $i$  (see figures 2 and 3). This correspondence however is deceptive, as one can easily show that equation (3) leads to infinitely large intercellular

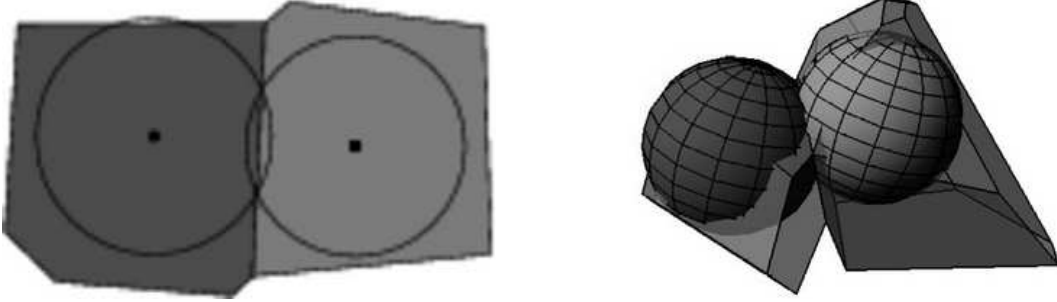


FIG. 3: Visualization of two intersecting circles (spheres) and their corresponding Voronoi domains in two (three) dimensions. Position and orientation of the Voronoi contact line (plane) coincides with the circle (sphere) intersection. The Voronoi surfaces are also determined by the positions of other cells (not shown here).

contact surfaces at the boundary of the convex hull of the points  $\{\mathbf{r}_i\}$ . In addition, in the case of a low cellular density the surfaces and volumes defined by the purely geometric approach (3) will evidently overshoot the actual cellular contact surfaces and volumes by orders of magnitude. On the other hand, Voronoi contact surfaces have been shown to approximate the cell shape in tissues remarkably well – at least in two-dimensional cross-sections [16]. Therefore, in order to have a contact surface estimate valid for different modeling environments we use a combination of the two approaches by setting

$$A_{ij} = \min \left\{ A_{ij}^{\text{sphere}}, A_{ij}^{\text{Voronoi}} \right\}. \quad (4)$$

This combination leads to upper bounds of intercellular contact surfaces on tissue boundaries and preserves the Voronoi surfaces within dense tissues by yielding a continuous transition between the two estimates. Depending on the local cellular deformations the difference can be in the range of 30% within dense tissues.

Note that equations (1) and (3) allow for different cell types by introducing varying radii, elastic moduli and receptor and ligand concentrations. All forces act in the direction of the normals to the next neighbors and on the center of the spheres. The total force on the cell  $i$  is then determined by performing a sum over the next neighbors  $\mathbf{F}_i = \sum_{j \in NN(i)} (F_{ij}^{\text{ad}} - F_{ij}^{\text{el}}) \mathbf{n}_{ij}$  and in addition we record the sum of the normal tensions

$$P_i = \sum_{j \in NN(i)} \frac{|\mathbf{F}_{ij} \mathbf{n}_{ij}|}{A_{ij}}, \quad (5)$$

where  $\mathbf{n}_{ij}$  denotes the unit vector pointing from cell  $i$  to cell  $j$ . The list of next neighbors is efficiently provided by the Delaunay triangulation. Once a force has been calculated, the

corresponding spatial step can be computed from the Langevin equation

$$m_i \ddot{\mathbf{r}}_i(t) = -\gamma_i \dot{\mathbf{r}}_i(t) + \mathbf{F}_i(t) \quad (6)$$

in the over-damped approximation  $m_i \ddot{\mathbf{r}}_i(t) \approx 0 \quad \forall i \quad \forall t$ , which is an adequate approximation for cell movement in medium [34] since the estimated Reynolds-numbers are extremely small [13]. Evidently, since additional adhesive bindings are at work, cellular movement in a tissue is even more damped [35].

The corresponding friction coefficient on a cell  $i$  is calculated from two distinct contributions  $\gamma_i = \gamma_i^{\text{visc}} + \gamma_i^{\text{ad}}$ , where the first results from the friction of a sphere in a fluid

$$\gamma_i^{\text{visc}} = 6\pi\eta R_i, \quad (7)$$

with  $\eta$  representing the effective viscosity of the medium or the extracellular matrix, respectively. The second is determined by adhesive forces with other cells and will therefore scale with the cell-cell contact surface

$$\begin{aligned} \gamma_i^{\text{ad}} = & \gamma^{\text{max}} \sum_{j \in NN(i)} A_{ij} \frac{1}{2} \left( 1 - \frac{\mathbf{F}_{ij} \cdot \mathbf{n}_{ij}}{|\mathbf{F}_{ij}|} \right) \times \\ & \times \frac{1}{2} \left( c_i^{\text{rec}} c_j^{\text{lig}} + c_i^{\text{lig}} c_j^{\text{rec}} \right), \end{aligned} \quad (8)$$

as illustrated in figure 4. A more exact approach would be to take differential cellular velocities into account (e. g. [13]) by including the drag force via

$$\dot{\mathbf{r}}_i = \frac{\sum_j (\mathbf{F}_{ij} + \gamma_{ij} \dot{\mathbf{r}}_j)}{\gamma_0 + \sum_j \gamma_{ij}}. \quad (9)$$

The corresponding treatment would necessitate the solution of  $3N \times 3N$  linear systems. In addition, one should keep in mind that within dense tissues many intercellular contacts are mediated by the extracellular matrix (with zero velocity). With using this approximations we assume that in average the elastic and adhesive interactions dominate the intercellular drag forces, i. e.  $F_{ij} \gg \gamma_{ij} \dot{\mathbf{r}}_i$ .

## B. Cellular parameters

In our model, cells have different internal states, which we chose to closely follow the cell cycle in order to make comparisons with experimental data as intuitive as possible.

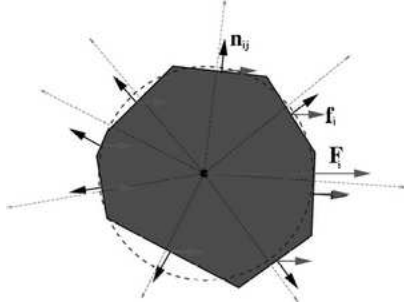


FIG. 4: The extent to which adhesive bonds contribute to friction depends on the direction of movement and on the contact surfaces. If total force and normal vector are parallel, the corresponding contact surface will not contribute at all to the friction coefficient in equation (8), whereas the contribution will be strongest with force and normal vector being antiparallel.

Consequently, the cellular status determines the actions of the cellular agents. We distinguish between 5 states:  $G_1$ -phase, S/ $G_2$ -phase, M-phase,  $G_0$ -phase, and necrotic.

During  $G_1$ -phase, the cell volume grows at a constant rate until the cell reaches its final mitotic size. Afterwards no further cell growth is performed. At the end of the  $G_1$ -phase a checkpointing mechanism is performed where the cell can switch into  $G_0$ -phase. If the cellular tension exceeds the threshold  $P^{\text{crit}}$  at this position in the cell cycle, the cell enters the  $G_0$ -phase, otherwise the cell enters the S/ $G_2$ -phase.

During the S-phase the DNA for the new cell division is synthesized, whereas during  $G_2$ -phase the quality of the produced DNA is controlled. In our model we do not distinguish between S-phase and  $G_2$ -phase. At the beginning of the phase the individual phase duration is determined using a normally-distributed random number generator [36] with a given mean and width. After this individual time has passed, the cells enter mitosis.

At the beginning of the mitotic phase – which lasts for about half an hour for most cell types – a mother cell divides and is replaced by two daughter cells. In the model these are slightly displaced in random direction, see subsection II C. Afterwards the daughter cells are left to their initially dominating repulsive forces (1). As in the S/ $G_2$ -phase the individual duration of the M-phase is determined using a normally-distributed random number generator. Afterwards the daughter cells enter the  $G_1$ -phase thus closing the cell cycle. Note that we do not differentiate between the internal phases of mitosis.

During  $G_0$ -phase, the cellular tension is monitored. Cells re-enter the cell cycle where they left it (i. e. at the beginning of the S/ $G_2$ -phase) if the cellular tension sinks below the critical threshold  $P^{\text{crit}}$ . Similar to the S/ $G_2$ -phase no growth is performed. Therefore in

our model, the difference between the S/G<sub>2</sub>-phase and the G<sub>0</sub>-phase is that the duration of the first phase is determined by the normally distributed individual time, whereas in the latter case the cellular tension is the determining factor. Consequently, the cells in G<sub>0</sub>-phase can serve as a reservoir of cells ready to start proliferating as soon as there is enough space available, which is common to many wound-healing models [10].

Intuitively, cells enter necrosis as soon as the nutrient concentration at the cellular position falls below a critical threshold. We study different mechanisms for the induction of necrosis within the model and will be able to rule out possible candidates (see subsection III A). Naturally, necrotic cells do not consume any nutrients and do slowly decay. In our model this is represented by removing these cells from the simulation at a rate  $r^{\text{necr}}$  – without performing prior shrinking.

Note that the only stochastic elements involved so far are the direction of mitosis and the durations of the M-phase and S/G<sub>2</sub>-phase. The first is required by the local assumption of isotropy, whereas the latter is required by the fact that proliferating cells having a common progenitor desynchronize rather quickly (usually after about 5 generations [37]): For these small systems of  $\mathcal{O}(2^5)$  cells mechanisms such as nutrient depletion or contact inhibition cannot explain the desynchronization.

### C. Proliferation

A cell will divide when the end of the S/G<sub>2</sub> phase has been reached. The initial direction of mitosis is chosen randomly from a uniform distribution on the unit sphere [36], which is the simplest possible assumption. Note however that since the cellular movement during the M-phase is not only determined by the mitotic partners but also by the surrounding cells the effective direction of mitosis may generally change during M-phase – depending on the configuration of the next neighbors. The radii of the daughter cells are decreased  $R^d = R^m 2^{-1/3}$  to ensure volume conservation and the daughter cells are placed at the distance  $d_{ij}^0 = R^m(1 - 2^{-1/3})$  to ensure that initially the deformations of surrounding cells do not change drastically. One should be aware that at this stage the forces calculated in equation (1) cannot represent the actual mitotic separation forces, since the considerable overlap  $h = R^m(2^{5/3} - 1)$  generates strong elastic forces in equation (1) which has then been applied far beyond its validity for small deformations. To the sake of simplicity we will not

use modified mitotic forces within this article. In addition, the relative shortness of the M-phase in comparison with the complete cell cycle leads to a small fraction of cells being in the M-phase. Therefore, we expect the consequences of our simplifying assumption to be relatively small. Anyway, to ensure for numerical stability, an adaptive step-size control has to be applied in the numerical solution of equation (6) – see the appendix.

#### D. Nutrient consumption and Cell Death

We view cells as bio reactors where oxygen and glucose react to waste products as lactose, water and carbon dioxide. The clean combustion of glucose would require the molar nutrient uptake rate of oxygen to be 6 times the molar glucose uptake rate:  $C_6H_{12}O_6 + 6O_2 \rightarrow 6H_2O + 6CO_2$ . However, for tumor tissue this cannot be the case as it is well-known that in the direct vicinity of tumors the concentration of lactic acid increases considerably which is a direct evidence for the incomplete combustion of glucose. By experimental estimations of average oxygen and glucose uptake rates for another cell line a considerable deviation from the ideal ratio has been found with about 1:1 [38]. Thus, in our model all viable cells consume oxygen and glucose diffusing in the surrounding extracellular matrix. This can be achieved by using the corresponding sink terms on the glucose and oxygen reaction-diffusion grids, respectively.

The nutrient uptake rates can in principle depend on the cell type, the local concentration of both nutrients, the existence of internal cellular nutrient reservoirs and many other factors. However, few information about the qualitative dependence is known: the rates in the literature (see e. g. [38]) are average values given in units of mol per seconds and volume of tissue since these data are obtained from whole cell populations without regard to the individual cell size, status and the local nutrient concentration. In addition, the functional form of the dependence is unknown as well. The simplest starting point is to assume that the nutrient uptake rates only depend – if at all – on the local nutrient concentration.

Depending on the cell type and on the local nutrient concentrations cells undergo apoptosis and/or necrosis when subject to nutrient depletion [25]. In this specific application we choose necrosis as the dominant pathway to cell death and neglect the effects of apoptosis though there is experimental evidence that these processes are linked with each other [39]. Necrotic cells are randomly removed from the simulation with a rate  $r^{\text{necr}}$ . The ef-

fect of apoptosis in the simulation would be similar, though apoptotic cells not break apart as necrotic cells but shrink and afterwards dissolve into small apoptotic bodies [40]. For the overall outcome of the total growth curve we expect insignificant changes by including apoptosis into the model.

With our computer simulation model we can test different hypotheses which critical parameters may influence the onset of necrosis: There could be two critical concentrations for both oxygen and glucose or just one combined parameter with an unknown dependence on the local concentrations. In addition, there could also be other processes such as necrotic waste material inducing apoptosis and/or necrosis, which will not be considered here.

### E. Nutrient distribution

We consider the case of avascular tumor growth and therefore assume that the transport of nutrients is performed passively by diffusion. Consequently, the diffusion through tumor tissue and also through the culture medium is described by a system of reaction-diffusion equations

$$\frac{\partial u^{\text{ox/gluc}}}{\partial t} = \vec{\nabla} \left[ D^{\text{ox/gluc}}(x) \vec{\nabla} u^{\text{ox/gluc}}(x, t) \right] - r^{\text{ox/gluc}}(x, t), \quad (10)$$

where  $u^{\text{ox/gluc}}(x, t)$  describes the local oxygen or glucose concentration,  $D^{\text{ox/gluc}}(x)$  the local effective oxygen or glucose diffusion coefficient and  $r^{\text{ox/gluc}}(x, t)$  the local oxygen or glucose consumption rate. In equation (10) we implicitly assume that the transport of matter can be described by an effective diffusion coefficient. This does not have to be the case, since cellular membranes pose complicated boundary conditions especially for larger molecules such as glucose. In addition, convection may also contribute to matter transport. Only if the tissue is isotropic on scales larger than a cell diameter this assumption is justified. Consequently, the discretization of equation (10) does only make sense on lattices with spacings exceeding the cellular diameters.

Though we use an effective diffusion coefficient  $D_{\text{eff}}$  it is sometimes necessary to allow for diffusivities varying on scales larger than the cell diameter – especially for larger molecules. For example, the effective diffusion coefficient of glucose is about  $700\mu\text{m}^2/\text{s}$  in water, whereas it is only  $100\mu\text{m}^2/\text{s}$  in tissue [41]. This effect is less pronounced for smaller molecules such

as oxygen with about  $2400\mu\text{m}^2/\text{s}$  in water and  $1750\mu\text{m}^2/\text{s}$  in tissue [42]. Consequently, when modeling in-vitro multicellular tumor spheroids one will have to take spatially varying diffusivities into account to appropriately model the nutrient concentrations on the spheroid boundary. In addition, varying diffusivities enable one to keep the rectangular shape of the diffusion grid which is favorable for the numerical solution, see also the appendix.

Another possibility would be to solve the nutrient diffusion within the spheroid only by assuming a spherical tumor symmetry with a time-dependent boundary moving with the spheroid size. However, with such an approach the spherical symmetry would not be an outcome but an intrinsic ingredient of the model. Consequently, in such a model the spheroid shape would not be of any comparative value.

Equation (10) does only have a defined solution if the initial conditions and the boundary conditions are set. Naturally, we chose in our simulations the initial and boundary concentrations to be equal, and their value was chosen in accordance with the experiment [25].

### III. RESULTS

#### A. Population Dynamics

The overall cell number is a parameter which can be quantified experimentally, either indirectly by simply calculating cell numbers from observed tissue volumes or directly by extensive automated cell-counting. In [25] the cell number has been determined indirectly for different concentrations of oxygen and glucose. With our model we have calculated growth curves for different nutrient concentrations and different hypotheses of nutrient uptake and necrosis induction. The simulations have been compared with four series of experimental data, where four different combinations of oxygen and glucose concentrations have been investigated. Naturally, within one set of simulations all parameters but the nutrient concentrations have been kept fixed.

We have tested the possibility that there exist critical concentrations for the two nutrients separately. However, in this case either the glucose or oxygen concentration dominantly limit the cell population dynamics. This does not reproduce the experimental data [25], since the growth curves for one of the nutrient concentrations being kept constant depend

strongly on the concentration of the other nutrient. Therefore, since low oxygen and large glucose concentrations can result in similar population dynamics as large oxygen and low glucose concentrations ([25]), both concentrations must enter the critical parameter. We have also tested the possibility of concentration-dependent nutrient consumption rates with the functional form of the Michaelis-Menten type kinetics

$$r^{\text{nut}} = r^{\text{min}} + \frac{(r^{\text{max}} - r^{\text{min}})C^{\text{nut}}}{C_{1/2} + C^{\text{nut}}}. \quad (11)$$

This model however uses many parameters that cannot be fixed with the present data. In addition, the values for  $C_{1/2}$  in the literature for oxygen-dependent proliferation [43] of 0.0083mM point into the direction that the oxygen consumption rates are always within the range of saturation, since the local oxygen concentration is always larger than 0.04 mM. Consequently, we have in the present model assumed constant cellular oxygen and glucose uptake rates for non-necrotic cells in the present model. We chose the product of oxygen and glucose concentration to be the limiting factor to sustain cellular viability. This simple ansatz did suffice to reproduce the experimental cellular growth curves (see figure 5). The best fit is achieved with the parameter set shown in table I. The corresponding tumor morphology is addressed in subsection III B.

Unfortunately, no error bars are given in [25] and the experimental data scatter considerably even on a logarithmic scale, see figure 5. Apart from the difficulty of establishing a defined experimental system in biology, this large scatter is also due to the necessity of destroying the spheroids during the measurements. Therefore, a whole ensemble of spheroids had to be measured. Since the monoclonality of these spheroids is not ensured, it is not a priori clear whether a single spheroid might contain several species or whether different spheroids might belong to different species with individual growth characteristics. In order to employ a procedure to minimize deviations between the simulation and experimental data we defined estimated error bars by calculating the difference to the artificial Gompertz growth curve

$$N(t) = N_0 \exp \left[ \frac{\alpha}{\beta} (1 - e^{-\beta t}) \right], \quad (12)$$

which has been shown to reproduce most growth processes in nature with remarkable accuracy [44].

Not every hypothesis on nutrient consumption and necrosis induction leads to acceptable agreement with experimental data – indicating the sensitivity of the model. The theoretical

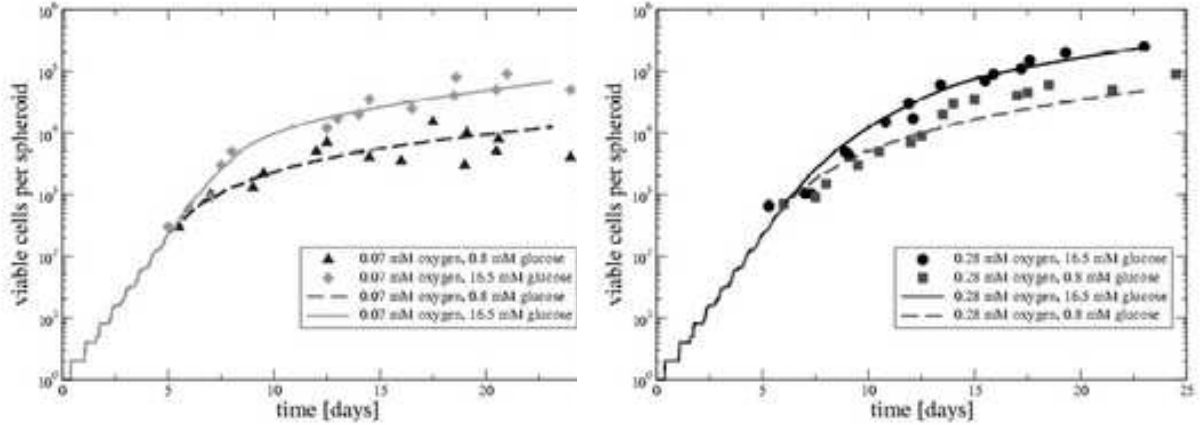


FIG. 5: Number of viable cells per spheroid for 0.8 and 16.5 mM glucose concentrations and either 0.07 mM oxygen concentration (left panel) or 0.28 mM oxygen concentration (right panel). Experimental data (symbols) were read off from [25], whereas lines correspond to the computer simulations.

predictions lie within the scattering region, see figure 5. Qualitatively, one can see that for all the simulations the initial exponential growth phase soon enters a crossover to a polynomial growth. In our model this crossover is due to two distinct mechanisms – contact inhibition and nutrient depletion – which lead to the similar outcome that after a certain time dominantly the spheroid surface will contribute to the proliferation, i. e.

$$\frac{dN}{dt} = \alpha N^{2/3}, \quad (13)$$

which has the polynomial solution  $N(t) = N_0 [1 + \beta t + \beta^2 t^2/3 + \beta^3 t^3/27]$  with  $\beta = \alpha/N_0^{1/3}$  [26]. Apart from the fact that necrosis is evidently more likely when nutrients are rare, the mechanisms cannot be clearly distinguished with a glance at the total growth curves in figure 5. However, since the mechanism of contact inhibition leads to cells resting in  $G_0$  rather than cells entering necrosis the differences can easily be analyzed in the cell cycle distribution. In figure 6 it is evident that for 0.07 mM oxygen and 0.8 mM glucose concentrations the nutrient starvation is the dominant limiting factor to cell cycle inhibition, since there are nearly no cells in  $G_0$ -phase and the majority of cells is necrotic. In the case of nutrient abundance (0.28 mM oxygen and 16.5 mM glucose) however, the majority of cells resides in  $G_0$ -phase, which is an indication for contact inhibition being the dominant reason for the crossover, as is also assumed in other models [10, 35]. This is also confirmed by the cross-sections of the

computer simulated tumor spheroids, see figure 7. Though in the case of nutrient abundance necrosis sets in much later, the number of necrotic cells rises at a much stronger slope and it is to be expected that necrosis will displace the contact inhibition as the major cause for surface-dominated growth after 25 days (with overall roughly  $5 \times 10^5$  cells involved, the simulations become very extensive and memory-consuming). Such a displacement of dominating mechanisms is already visible for some intermediate nutrient concentrations. For example, in the case of 0.07 mM oxygen and 16.5 mM glucose concentrations the number of cells in G<sub>0</sub>-phase first rises to reach its maximum after 10 days and afterwards decays in combination with a strong rise in necrotic cells (figure 6, upper right panel). Such a behavior is not observed in the regime of large oxygen and low glucose concentrations, where necrosis and contact inhibition set in simultaneously and nutrient starvation is the main limiting factor. This is due to the considerably decreased glucose diffusion coefficient in tumor tissue, whereas the diffusion coefficient of oxygen is nearly the same in tissue and water, compare subsection II E. Consequently, the already low glucose concentration of 0.8 mM at the boundary drops rapidly when the number of tumor cells increases, since new glucose supply diffuses very slow from the outside.

## B. Tumor Spheroid Morphology

To estimate the quality of a mathematical model one has to find experimentally accessible parameters. This is especially difficult when thinking about tissue morphology, since very often the patterns are hard to quantify in terms of numbers. The morphology of three-dimensional tumor spheroids is rather simple: An inner necrotic core is surrounded by a layer of quiescent cells, which is in turn surrounded by the outer layer of proliferating cells. Qualitatively, this morphology is well reproduced in the case of initial nutrient abundance, see right panels in figure 7. In the case of nutrient starvation however there is virtually no layer of quiescent cells (figure 7 left panels), as contact inhibition is not of importance in this scenario (see figure 6). It is evident from figure 7 that the size of the layers depends on the boundary concentrations. In addition, it also depends on the nutrient consumption rates and diffusivities of oxygen and glucose within the tumor tissue. The size of the necrotic core is also very sensitive on the rate at which necrotic cells are being removed from the simulation.

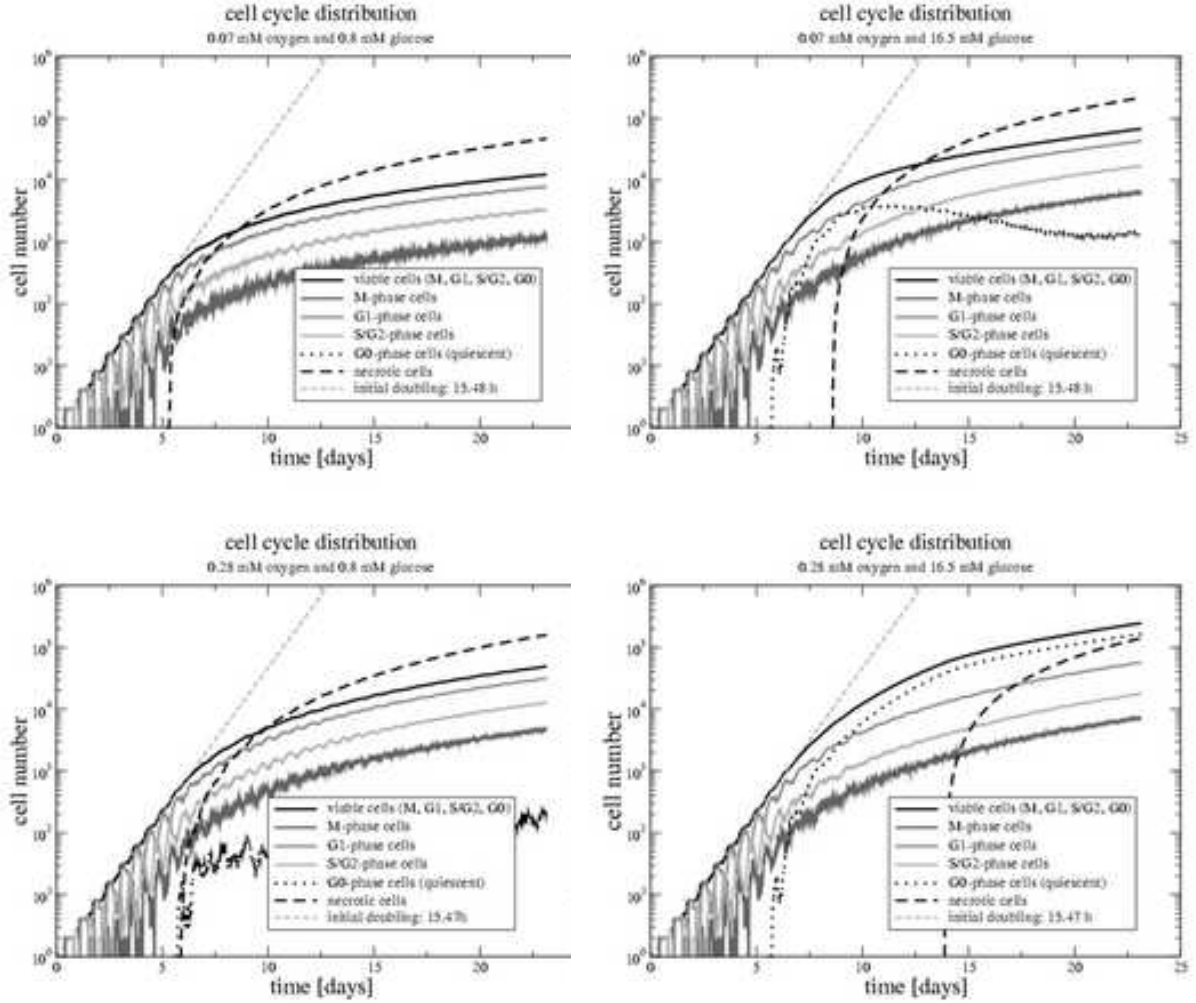


FIG. 6: Cell cycle distribution for different oxygen and glucose concentrations. Depending on the external nutrient concentrations, significant differences mark the dominance of different mechanisms to limit the cell cycle. Fits to the regions of exponential growth – marked by the complete absence of necrotic and quiescent cells – reproduce the shortest observed cycle time within statistical fluctuations.

Note that in the spheroid cross-sections it is evident that – if oxygen and/or glucose are limited – a relatively small number of cells with constant nutrient uptake rates suffices to drop the nutrient levels under the critical threshold thus leading to the onset of necrosis and the absence of a layer of quiescent cells in the end of the simulations, compare also figure 6. This is different for a model with concentration or cell-cycle dependent nutrient uptake rates. In the first case the absolute value of the nutrient concentration gradients would be decreased thus giving rise to a broader viable layer which – in turn – could allow for the existence of

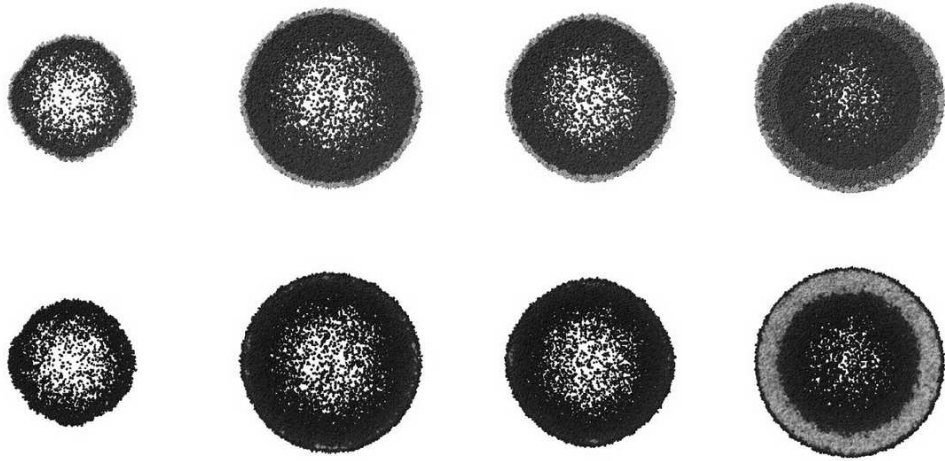


FIG. 7: Cross-section of computer-simulated tumor spheroids after 23 days of simulation time. The first row shows the cellular status (necrotic cells in dark grey, quiescent cells in grey, cells in the cell cycle in light grey), whereas the second row visualizes the cellular tension (free cells in dark grey, cells under strong pressure in light grey). Nutrient concentrations from left to right are given by 0.07 mM oxygen and 0.8 mM glucose, 0.07 mM oxygen and 16.5 mM glucose, 0.28 mM oxygen and 0.8 mM glucose, and 0.28 mM oxygen and 16.5 mM glucose, respectively.

a quiescent layer. In the second case the intermediate emergence of cellular quiescence (see figure 6) would also decrease the absolute value of the nutrient concentration gradient towards the necrotic core, which would prolong and eventually stabilize the existence of a quiescent layer also for nutrient depleted configurations. Therefore, in order to distinguish between nutrient uptake models, the tumor spheroid morphology is an important criterion, whereas the simple total growth curve is not sufficient to make quantitative predictions about the mechanisms at work.

Interestingly, the spheroids in figure 7 are fairly round, especially for the case where nutrients are provided in abundance. This is due to the stochastic nature of the mitotic direction which forces initial differences to average out after some time – which can easily be verified by restarting the computer code with similar parameters but different seed values for the random number generator (data not shown). This is in agreement with many spheroids observed in the experiment [25] and in other computer simulations [35]. However, the spheroids are less spherical for extreme nutrient depletion, since firstly the small cell number yields less stochastic events that contribute to the averaging and secondly the

emergence of localized holes in the necrotic core is not counterbalanced by a strong mainly isotropic proliferative pressure from the proliferating rim – as is the case for large nutrient concentrations. The sometimes observed deviations from the spherical form [25] can also have additional reasons: The spheroids might be hetero-clonal while all cells in our simulation are assumed to be monoclonal. If a spheroid does not develop from a single but two genetically differing cells, these cells might exhibit different growth characteristics.

### C. Parameter Dependence

The growth curves shown in figure 5 have been calculated using the – comparably many – parameters in table I. However, since mainly deterministic and rather physically-motivated interactions are assumed, more parameters than in PDE or cellular automaton models can be accessed by independent experiments and do not need to be varied as fit parameters. Some of these parameters deserve special attention: The elastic parameters of EMT6/Ro tumor cells might differ from those in table I (compare e. g. [10, 43]), which could give rise to a misestimate of the elastic forces by about 30 percent. An initial cycle time of 17h has been obtained in [25] using a Gompertz fit to the spheroid volume. This fit had been applied to already existing small spheroids that may exhibit growth retardation effects. Therefore – and in order to reproduce the slopes correctly – we have used a slightly decreased shortest possible cycle. The cell tension defined here is simply a sum over all normal tensions with the next neighbors. The value that we have obtained as fit parameter is about 6 times as large as the critical cellular compression used as a criterion for contact inhibition in similar simulations (90 Pa in [10]). In part, this may be due to the Voronoi surface correction – surfaces tend to be smaller than sphere surfaces – which leads to generally larger normal tensions. The remaining difference should be attributed to the fact that we use a different cell line.

In accordance with the assumption of contact inhibition being the dominant cause for the crossover from exponential to polynomial growth in the case of nutrient abundance, the initial phases of the theoretical growth curve for 0.28 mM oxygen and 16.5 mM are dominantly dependent on the critical cell tension, whereas the other growth curves – especially for nutrient depletion – strongly depend on the nutrient uptake rates and the necrotic parameter. Generally, the late stages of spheroid growth depend critically on the nutrient-related

parameter	value	unit	comment
ECM viscosity $\eta^{\text{VISC}}$	$5 \cdot 10^{-3}$	kg/( $\mu\text{ms}$ )	[10], estimate
adhesive friction $\gamma^{\text{max}}$	0.1	kg/( $\mu\text{m}^2\text{s}$ )	[10], estimate
receptor concentration $c^{\text{rec}}$	1.0	#	fixed
ligand concentration $c^{\text{lig}}$	1.0	#	fixed
oxygen diffusivity $D_{\text{eff,ox}}^{\text{tissue}}$	1750.0	$\mu\text{m}^2/\text{s}$	[42]
glucose diffusivity $D_{\text{eff,gluc}}^{\text{tissue}}$	105.0	$\mu\text{m}^2/\text{s}$	[41]
mitotic phase $\tau^{\text{m}}$	$(3.6 \pm 0.9) \cdot 10^3$	s	estimate
S/G <sub>2</sub> -phase $\tau^{\text{S/G}_2}$	$(18.0 \pm 7.2) \cdot 10^3$	s	estimate
shortest cycle time $\tau_{\text{min}}$	$54.0 \cdot 10^3$	s	[25], estimate
mitotic cell radius $R^{\text{m}}$	5.0	$\mu\text{m}$	estimate
cell elastic modulus $E$	$1.0 \cdot 10^{-3}$	MPa	[10], estimate
cell Poisson number $\nu$	0.5	#	assumption
adhesive coefficient $f^{\text{ad}}$	$1.0 \cdot 10^{-4}$	$\mu\text{N}/\mu\text{m}^2$	eq. overlap
necrosis absorption rates $r^{\text{necr}}$	$2.0 \cdot 10^{-6}$	cells/s	estimate/fit
critical cell tension $P^{\text{crit}}$	$0.6 \cdot 10^{-3}$	MPa	fit parameter
oxygen uptake $r^{\text{ox}}$	20.0	$10^{-18}$ mol/(cell s)	fit parameter
glucose uptake $r^{\text{gluc}}$	95.0	$10^{-18}$ mol/(cell s)	fit parameter
critical product $p^{\text{oxgluc}}$	0.025	mM <sup>2</sup>	fit parameter

TABLE I: Best fit model parameters that are used in the simulations shown in figure 5.

See text for explanations.

parameters.

Note that in the over-damped approximation of equation (6) the solution is calculated as a ratio of combined elastic and adhesive forces to a friction parameter, which is largely influenced by cell-cell adhesion. Therefore, the model will not be very sensitive on the specific adhesion coupling constants and the adhesion-determined friction, as rather their ratio is mainly influencing the model behavior as long as elastic forces are small.

#### D. Saturation of growth curves

A complete saturation of the cell number or spheroid size – as suspected by [25] and others [24] – cannot be reproduced in the computer simulations with the parameters in table I. The large scatter of the data in the case of nutrient depletion (figure 5 left panel) does not exhibit a clear saturation within 25 days, which is not reached in the other configurations anyway. For the explanation of a growth saturation the nature of the additional mechanism remains controversial. For example, in [24] an effective movement of cells towards the necrotic core has been observed leading to the assumption of a chemotactic signal secreted by necrotic cells. The corresponding computer simulations in [7] did lead to saturation. Since it is somewhat arbitrary to assume that tumor cells follow a necrotic signal we also tested a simpler hypothesis:

In figure 7 macroscopic holes are visible within the necrotic core – created by the removal of necrotic cells from the simulation. Once such a hole is established, it even tends to grow, since the intercellular adhesion is of very short range. (Recall that equation (2) depends on the contact surface.) We have found that an increase of adhesive normal forces to  $f^{\text{ad}} = 0.0003\mu\text{N}/\mu\text{m}$  suffices to close the visible holes completely – thereby inevitably coupling the proliferating ring to the necrotic core. Consequently, the volume loss generated by removing necrotic cells with a certain rate must be balanced by a movement of proliferating or quiescent cells from the outer layers into the necrotic core. In addition, the outward component of the proliferative pressure on the outer layer is counterbalanced by the increased cellular adhesion as well. For such a system, a growth saturation is inevitable: As in the late stages of spheroid growth the cellular birth rate can be assumed to be proportional to the spheroid surface  $R_{\text{birth}} \approx \alpha N^{2/3}$  and the rate of cell removal is proportional to the number of necrotic cells residing in the center, the total cell number can be described by

$$\frac{dN}{dt} = \alpha N^{2/3}(t) - \beta [N(t) - \gamma N^{2/3}(t)] \quad (14)$$

with  $\alpha, \beta, \gamma$  being positive constants. The solution of this equation always reaches the steady state  $N_{\infty} = \left(\frac{\alpha}{\beta} + \gamma\right)^3$ , which is stable for  $\beta > 0$ . Therefore, in this regime the nutrient depletion is the dominant factor limiting tumor spheroid growth.

A pseudo-Brownian cellular motion might increase the range of cellular adhesion. We incorporated this by adding to every coordinate a normally-distributed cellular displacement of mean  $0\mu\text{m}$  and width  $\sigma_i = \sqrt{2D^{\text{cell}}\delta t}$ , with  $D^{\text{cell}} \approx 0.0001\mu\text{m}^2/\text{s}$  being an effective cellular

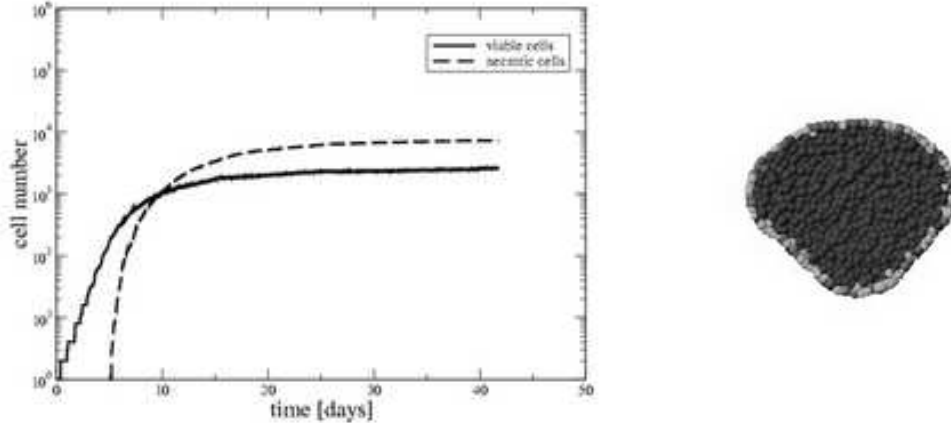


FIG. 8: After assuming an increased adhesive coupling the emergence of holes within the necrotic core is completely inhibited. Consequently, a steady-state flow equilibrium is established leading to growth saturation of the spheroid (left). No further mechanisms need to be assumed. The assumption of a small Pseudo-Brownian motion does not alter the result, but smoothes the transition from exponential growth to saturation. In addition, the fast closure of holes in the necrotic core can lead to deviations from the spherical symmetry (right). As before, cells in the cell cycle are marked in light grey, quiescent cells in grey and necrotic cells are depicted by dark grey.

diffusion constant. It turned out that the transition from exponential growth to saturation becomes smoother. We conclude that growth saturation of both cell number and spheroid radius in off-lattice computer simulations can be reached by assuming increased intercellular adhesion forces, where a pseudo-Brownian cellular motion only smoothes the transition, see figure 8. The assumption of some diffusing signal as in [7] is not necessary. Interestingly, during the period of saturation, deviations from the spherical shape can emerge: The position of unstable intermediate holes within the necrotic core is randomly distributed and gives rise to macroscopic deviations from spherical shape on the spheroid surface. Therefore, an irregular spheroid shape can also be explained by individual durations of the necrotic process. Note that another candidate for a cell loss mechanism is shedding of cells at the spheroid surface [45]. All these mechanisms might could be combined with an involvement of metabolic waste products in the induction of necrosis.

## IV. SUMMARY

We have demonstrated that the Voronoi/Delaunay hybrid model can very well be used to establish agent-based cell-tissue simulations. The Voronoi/Delaunay approach provides some advantages: Firstly, compared to the description of cells by deformable spheres, the Voronoi tessellation provides an improved estimate of contact surfaces within dense tissues. The present model combines the advantages of both model concepts. Secondly, the weighted Delaunay triangulation is an efficient method to determine neighborhood topologies for differently-sized sphere-like objects. In addition, it can efficiently be updated in the case of moving objects. The model is very rich in features and therefore allows many comparisons with the experiments. It can easily be combined with established models on intercellular adhesion and cellular elasticity that rely on direct experimental observables. Therefore it allows some of its parameters to be fixed by independent experiments. The parameters which had to be determined with respect to macroscopic quantities represent existing physical quantities. Since such quantities can be falsified in future experiments, the model provides predictive power to a greater extent than differential equation or cellular automaton approaches.

Unlike previous models [7, 35, 46] – which only considered the influence of one nutrient on the dynamics of three-dimensional multicellular tumor spheroids – we were able to reproduce the experimental growth curves with a single parameter set by considering the spatiotemporal dynamics of both the oxygen and glucose concentrations simultaneously. A saturation of growth could be obtained by increasing intercellular adhesive forces threefold.

On the one hand, the typical spheroid morphology is reproduced qualitatively very well. On the other hand, a quantitative reproduction not only of cell population growth curves but also of spheroid morphology could allow for a more detailed analysis of nutrient consumption models: For a different cell line an oxygen : glucose uptake ratio of about 1:1 has been found [38]. In contrast, our computer simulations point to the scenario that the oxygen consumption rates are much smaller (about 1:5) than the glucose consumption rates (table I), though the values are within the ranges of uptake rates in the literature if considered separately. This discrepancy may be due to several reasons. Firstly, such a ratio of oxygen and glucose uptake might actually be the case for EMT6/Ro cells. Secondly, the effective diffusivities within tissue for oxygen and glucose obtained from [42] and [41] might not be

correct – this would lead to different currents of oxygen and glucose within the spheroid. Thirdly, the model assumptions of roughly constant nutrient uptake rates and the product of both concentrations being the critical parameter for necrosis might not be correct.

We have seen that the quantitative analysis of the overall growth curve can in principle be used to determine unknown parameters. The current experimental data however exhibit too much scatter to determine parameters with accuracy, therefore a combined experimental and theoretical investigation of multicellular tumor spheroids of a single well-defined cell line is of urgent interest.

The presented model is especially suitable for systems with a comparably large number of cells. In addition, it supports different cell types as well. The cell shape however, is restricted to convex cells. This makes it suitable to model rather dense cell tissues such as e. g. epithelia where one can investigate the roles of differential adhesion, elastic interactions and active cellular migration in tissue flow equilibrium. Further applications of the Voronoi/Delaunay method will therefore include the modeling of epithelia, bone formation, and bio films. In addition, the weighted Delaunay triangulation is a suitable tool for the modeling of boundary conditions e. g. in froths.

## V. ACKNOWLEDGMENTS

G. Schaller is indebted to T. Beyer and W. Lorenz for discussing many aspects of the algorithms and testing the code. J. Galle is being thanked for his advice on cellular interactions. G. Schaller was supported by the SMWK. M. Meyer-Hermann was supported by a Marie Curie Intra-European Fellowship within the Sixth EU Framework Program.

## VI. APPENDIX

### A. Program Architecture

The programming language *C++* supports object-oriented programming and thus enables us to identify individual cells with instantiations of objects. These objects are stored in a list to allow for efficient deletion (apoptosis or necrosis) and insertion (proliferation). We had already implemented a weighted kinetic and dynamic Delaunay triangulation in three dimensions [15] which provides – once calculated – constant average access to the next

neighbors for differently sized spheres. This is achieved by using pointers on cells as the objects in the weighted Delaunay triangulation and storing the triangulation vertices in the cell objects. The Voronoi tessellation – which is the geometric dual of the Delaunay triangulation – provides the three-dimensional contact surface corrections.

If the spatial steps are not too large, the neighborhood can be updated over the time with in average linear effort, i. e. the time necessary to update the neighborhood relations after movement scales linearly with the number of cells. This limitation can be safely ensured by an adaptive step size algorithm in the numerical solution of equation (6). In our simulations, the average time step size was around 30 s thus leading to roughly 60000 time steps for 23 days of simulation time. At every time step the list of cells is iterated and for every cell all new variables are calculated. Afterwards the cellular parameters are synchronized. Note that discontinuous events such as cell proliferation and cell death correspond to insertion/deletion of just one cell in the list and become valid in the next time step. The Delaunay triangulation and the diffusion grid are then updated with the cellular displacements and radius changes or nutrient consumption rates, respectively. Therefore, all coupled equations are solved synchronously by storing the solution of every equation until the solutions of all equations have been calculated.

## B. Cellular kinetics

In the over-damped approximation, the cellular equation of motion (6) transforms into

$$\dot{\mathbf{r}}_i(t) = \frac{1}{\gamma_i} \mathbf{F}_i(t), \quad (15)$$

which is just a first order differential equation that can easily be solved numerically. There is a variety of established numerical algorithms to choose from and we decided to stick with a simple forward-time discretization – which is just a first order method. The first reason for this is that the uncertainties arising from the cell model presumably exceed the numerical errors by orders of magnitude. In addition, higher order methods such as e. g. Runge-Kutta require intermediate evaluations of the forces. In our model however this would necessitate intermediate refinements of the triangulation thus considerably increasing the numerical complexity. Multi-value Predictor-Corrector methods are also not suitable, since in the present model the intercellular forces are not continuous, especially during mitosis. Keeping

these arguments in mind one still has to guarantee numerical stability of the results. This can be achieved by using an adaptive time step size. In order to avoid slope calculations we chose a small time step if the spatial step sizes exceeded a critical value, which was always chosen much smaller than the cellular radius.

### C. Reaction-Diffusion Equation

Three-dimensional reaction-diffusion equations often constitute a significant challenge for present computational hardware since for a reasonable resolution a large number of lattice points is needed. In addition, not every algorithm is numerically stable. For example, the ADI algorithm is numerically stable in two dimensions but not in three [47]. Therefore there exist time step limitations on the solution of the full time-dependent problem (10).

If the diffusion coefficients and the considered time steps are comparably large, the steady-state approximation  $\frac{\partial u}{\partial t} \approx 0$  can be applied and by neglecting the time dependencies equation (10) reduces to a Helmholtz problem

$$\left[ \vec{\nabla} D(x) \right] \left[ \vec{\nabla} u(x) \right] + D(x) \vec{\nabla}^2 u(x) = r(x). \quad (16)$$

The steady-state-approximation has already been applied in e. g. [46]. Equation (16) can be solved numerically with comparably low computational effort and – more important – with numerically stable methods. The methods to solve (16) differ significantly in their convergence time. A simple relaxation method such as Jacobi or Gauss-Seidel [47] does not converge fast enough. In case of spatially constant diffusion coefficients the Fast Fourier Transform can be employed. Tumor tissue however, does have a different diffusivity than agar [38, 48] which made us favor a Vcycle-Multi-grid algorithm that uses Gauss-Seidel relaxation [49].

Since the discretization of equations (10) and (16) is done on a simple  $64 \times 64 \times 64$  cubic lattice with a lattice constant of  $15.625 \mu\text{m}$  – which is larger than the cellular diameter – and as the cell positions are arbitrary in our off-lattice model, we do use a tri-linear interpolation

to determine the local concentration from the concentrations on the eight closest lattice nodes

$$\begin{aligned}
f(x, y, z) = & f_{000}(1-x)(1-y)(1-z) \\
& + f_{100}x(1-y)(1-z) + f_{010}(1-x)y(1-z) \\
& + f_{001}(1-x)(1-y)z \\
& + f_{110}xy(1-z) + f_{101}x(1-y)z \\
& + f_{011}(1-x)yz + f_{111}xyz,
\end{aligned} \tag{17}$$

where  $f_{ijk}$  represent the values of the function  $f$  on the corners of a cube of length 1. The reaction rates created by the cells are handled similarly by distributing them on the closest lattice nodes. The local diffusion coefficients can be set by the tumor cells according to their spatial position. This approximates the correct boundary conditions. The size of the diffusion grid was with  $1000^3 \mu\text{m}^3$  always completely enclosing the tumor spheroids and by direct observation of the nutrient isosurfaces it was made sure that the rectangular boundary conditions did not influence the spheroidal concentration isosurfaces in the vicinity of the tumor spheroid.

#### D. Fitting experimental data

In order to minimize the difference between theoretical and experimental observables we performed roughly 150 computer simulations over a wide range of parameters until the visual agreement with the experiment was satisfactory. Afterwards we started Powells method [47] with several perturbations around this optimal parameter set by minimizing the squared differences of the logarithms of theoretical and experimental growth curves, i. e.

$$\chi^2 = \sum_{i:\text{exp}} \sum_{j:\text{meas}} \frac{1}{\sigma_{ij}^2} [\ln N_{ij}^{\text{exp}} - \ln N_{ij}^{\text{sim}}[p_1, p_2, \dots]]^2, \tag{18}$$

where the  $p_\alpha$  are the parameters that have been varied and the errors of the experimental data points  $\sigma_{ij}$  have been estimated by calculating the difference to a Gompertz growth curve. Note that it is a purely geometric and therefore deterministic algorithm, which opens the possibility that it will terminate within a local minimum. In order to decrease the probability of terminating within a local minimum, several runs should be performed. However, the changes of parameters are negligible, since due to the strong scatter of the

data the visual data fit is satisfactory already.

---

- [1] J. D. Murray, *Mathematical Biology*, vol. 17 of *Interdisciplinary Applied Mathematics* (Springer, Berlin Heidelberg, 2002), 3<sup>rd</sup> ed.
- [2] N. M. Shnerb, Y. Louzoun, E. Bettelheim, and S. Solomon, *Proceedings of the National Academy of Sciences* **97**, 10322 (2000).
- [3] E. Bettelheim, O. Agam, and N. M. Shnerb, *Physica E* **9**, 600 (2001).
- [4] A. Deutsch, *Informatik in den Biowissenschaften* pp. 181–192 (1993).
- [5] D. Drasdo, S. Dormann, S. Hoehme, and A. Deutsch, *Cell-based models of avascular tumor growth* (Birkhäuser, Basel, 2003).
- [6] M. Meyer-Hermann, *Journal of Theoretical Biology* **216**, 273 (2002).
- [7] S. Dormann and A. Deutsch, *In Silico Biology* **2**, 393 (2002).
- [8] T. Beyer, M. Meyer-Hermann, and G. Soff, *International Immunology* **14**, 1369 (2002).
- [9] D. Drasdo, R. Kree, and J. S. McCaskill, *Physical Review E* **52**, 6635 (1995).
- [10] J. Galle, M. Loeffler, and D. Drasdo, *Biophysical Journal* (2004), submitted.
- [11] E. Palsson and H. G. Othmer, *Proceedings of the National Academy of Sciences* **97**, 10448 (2000).
- [12] E. Palsson, *Future Generation Computer Systems* **17**, 835 (2001).
- [13] J. Dallon and H. G. Othmer, *Journal of Theoretical Biology* (2004), submitted.
- [14] H. Honda, M. Tanemura, and A. Yoshida, *Acta Biotheoretica* **48**, 121 (2000).
- [15] G. Schaller and M. Meyer-Hermann, *Computer Physics Communications* (2004), to appear.
- [16] H. Honda, *Journal of Theoretical Biology* **72**, 523 (1978).
- [17] F. Graner and J. A. Glazier, *Physical Review Letters* **69**, 2013 (1992).
- [18] N. J. Savill and J. A. Sherratt, *Developmental Biology* **258**, 141 (2003).
- [19] E. L. Stott, N. F. Britton, J. A. Glazier, and M. Zajac, *Mathematical and Computer Modelling* **30**, 199 (1999).
- [20] S. Turner and J. A. Sherratt, *Journal of theoretical Biology* **216**, 85 (2002).
- [21] M. Meyer-Hermann and P. K. Maini, submitted (2004).
- [22] M. Weliky and G. Oster, *Development* **109**, 373 (1990).
- [23] M. Weliky, G. Oster, S. Minsuk, and R. Keller, *Development* **113**, 1231 (1991).

- [24] J. Folkman and M. Hochberg, *The Journal of Experimental Medicine* **138**, 745 (1973).
- [25] J. P. Freyer and R. M. Sutherland, *Cancer Research* **46**, 3504 (1986).
- [26] W. Mueller-Klieser, W. Schreiber-Klais, S. Walenta, and M. H. Kreuter, *International Journal of Oncology* **21**, 1307 (2002).
- [27] H. Hertz, *J Reine Angewandte Mathematik* **92**, 156 (1882).
- [28] L. D. Landau and E. M. Lifshitz, *Theory of Elasticity* (Pergamon Press, London, 1959).
- [29] C. Wei, P. M. Lintilhac, and J. J. Tanguay, *Plant Physiology* **126**, 1129 (2001).
- [30] W. Alt and T. T. Tranquillo, *J. Biol. Syst.* **3**, 905 (1995).
- [31] D. E. Ingber, *Journal of Cell Science* **116**, 1157 (2003).
- [32] D. E. Ingber, *Journal of Cell Science* **116**, 1397 (2003).
- [33] A. Okabe, B. Boots, K. Sugihara, and S. N. Chiu, *Spatial tessellations: Concepts and applications of Voronoi diagrams*, Probability and Statistics (Wiley, NYC, 2000), 2<sup>nd</sup> ed.
- [34] J. Howard, *Mechanics of Motor Proteins and the Cytoskeleton* (Sinauer Associates, Inc., 23 Plumtree Road Sunderland MA 01375 U.S.A., 2001).
- [35] D. Drasdo and S. Höhme, *Mathematical and Computer Modelling* **37**, 1163 (2003).
- [36] B. M. Gammel, *Matpack C++ Numerics and Graphics Library*, <http://www.matpack.de/> (2003).
- [37] J.-U. Kreft, G. Booth, and J. W. T. Wimpenny, *Microbiology* **144**, 3275 (1998).
- [38] L. A. Kunz-Schughart, J. Doetsch, W. Mueller-Klieser, and K. Groebe, *Am. J. Physiol. Cell. Physiol.* **278**, 765 (2000).
- [39] H. S. Bell, I. R. Whittle, M. Walker, H. A. Leaver, and S. B. Wharton, *Neuropathology and Applied Neurobiology* **27**, 291 (2001).
- [40] B. Noble, *European Cells and Materials* **6**, 46 (2003).
- [41] J. J. Casciari, S. V. Sotirchos, and R. M. Sutherland, *Cancer Research* **48**, 3905 (1988).
- [42] J. Grote, R. Susskind, and P. Vaupel, *Pflugers Arch.* **372**, 37 (1977).
- [43] T. Roose, P. A. Netti, L. L. Munn, Y. Boucher, and R. K. Jain, *Microvascular Research* **66**, 204 (2003).
- [44] Y. Ling and B. He, *IEEE Transactions on Biomedical Engineering* **40**, 1193 (1993).
- [45] J. Landry, J. P. Freyer, and R. M. Sutherland, *Cell Tissue Kinetics* **15**, 585 (1982).
- [46] K. Groebe and W. Mueller-Klieser, *International Journal of Radiation Oncology Biology Physics* **34**, 395 (1996).

- [47] W. H. Press, S. A. Teukolsky, W. T. Vetterling, and B. P. Flannery, *Numerical Recipes in C* (Cambridge University Press, 1994), 2<sup>nd</sup> ed.
- [48] J. P. Freyer and R. M. Sutherland, *Cancer Research* **46**, 3513 (1986).
- [49] W. L. Briggs, V. E. Henson, and S. F. McCormick, *A multigrid tutorial* (Society for Industrial and Applied Mathematics, 2000), 2<sup>nd</sup> ed.